Article

Probing the Interplay between Dendritic Spine Morphology and Membrane-Bound Diffusion

Max Adrian,[1] Remy Kusters,[2] Cornelis Storm,[2,3] Casper C. Hoogenraad,[1] and Lukas C. Kapitein[1,*]
[1]Division of Cell Biology, Faculty of Science, Utrecht University, Utrecht, the Netherlands; [2]Department of Applied Physics and [3]Institute for Complex Molecular Systems, Eindhoven University of Technology, Eindhoven, the Netherlands

ABSTRACT   Dendritic spines are protrusions along neuronal dendrites that harbor the majority of excitatory postsynapses. Their distinct morphology, often featuring a bulbous head and small neck that connects to the dendritic shaft, has been shown to facilitate compartmentalization of electrical and cytoplasmic signaling stimuli elicited at the synapse. The extent to which spine morphology also forms a barrier for membrane-bound diffusion has remained unclear. Recent simulations suggested that especially the diameter of the spine neck plays a limiting role in this process. Here, we examine the connection between spine morphology and membrane-bound diffusion through a combination of photoconversion, live-cell superresolution experiments, and numerical simulations. Local photoconversion was used to obtain the timescale of diffusive equilibration in spines and followed by global sparse photoconversion to determine spine morphologies with nanoscopic resolution. These morphologies were subsequently used to assess the role of morphology on the diffusive equilibration. From the simulations, we could determine a robust relation between the equilibration timescale and a generalized shape factor calculated using both spine neck width and neck length, as well as spine head size. Experimentally, we found that diffusive equilibration was often slower, but rarely faster than predicted from the simulations, indicating that other biological confounders further reduce membrane-bound diffusion in these spines. This shape-dependent membrane-bound diffusion in mature spines may contribute to spine-specific compartmentalization of neurotransmitter receptors and signaling molecules and thereby support long-term plasticity of synaptic contacts.

INTRODUCTION

Dendritic spines are subcellular compartments that protrude from the dendritic shaft and typically consist of a micron-sized head connected to the dendrite by a thin neck (1). Importantly, spine morphology is neither homogenous nor static. Changes in spine morphology over time have been linked to neuronal activity and learning paradigms both in vitro and in vivo (2–4). The maturation of spines, from filopodia to mature mushroom-shaped spines with a large postsynaptic density (PSD) in the head, has been described in Mattison et al. (5) and Hu and Hsueh (6), explaining the large variety of spine shapes along a dendrite. Importantly, spine size has also been correlated to synaptic strength—a measure often based on the number of glutamate receptors located in the spine and integrated into the PSD (7). These receptors can reach the synapse either through lateral diffusion in the plasma membrane or by local exocytosis from intracellular storage pools (8).

Many studies have characterized the motility and retention of glutamate receptors in spines (9–13). In addition, theoretical calculations and numerical simulations have suggested that the morphology of spines may alter the capturing and compartmentalization of glutamate receptors and other membrane-bound proteins (14–19). Compartmentalization in spines has already been observed both for electrical stimuli (20,21) and cytoplasmic diffusion (22–24). For both, mushroom-like spines have shown less coupling to the dendritic shaft. Less clear is the role of spine morphology in membrane-bound diffusion. Early studies showed that mushroom-like spines equilibrate more slowly after bleaching fluorescent markers in the membrane than do the stubby spines (25,26). It was also shown that spines can retain membrane-associated signaling molecules like the small GTPase Ras, preventing them from spreading along the dendrite (27). Similarly, it has been demonstrated that the spine neck can hamper diffusion into spines (28). However, despite the evidence that membrane-bound diffusion is altered in mushroom-shaped spines, it has remained unclear to what extent these effects are purely due to the shape of the spine or to specific barriers in the spine neck that hinder diffusion.

CrossMark

Previously, we and others have modeled how morphology alone could affect the lateral diffusion within spines (14,17–19). This revealed that the neck diameter may play a role in regulating diffusion speed. However, dendritic spines are too small to measure accurately with conventional fluorescent microscopy, necessitating the use of superresolution microscopy to directly correlate diffusion time constants with morphology parameters (29). Here we use single molecule localization microscopy and photoconversion of a small exogenous membrane-bound probe to accurately quantify spine morphology and diffusion rates. To explore the contribution of spine morphology to the timescale of membrane-bound diffusion out of spines, we then compare the diffusion measurements with particle simulations carried out on the same morphologies. We find that the overall shape of the spine does influence diffusion as expected from simulations. However, many spines showed slower diffusion than expected, purely based on spine shape; this indicates that other biological confounders influence membrane-bound diffusion in these spines.

MATERIALS AND METHODS

Ethics statement

All animal experiments were performed in compliance with the guidelines for the welfare of experimental animals issued by the Government of The Netherlands and approved by the Animal Ethical Review Committee of Utrecht University.

Neuron culture and transfection

Primary hippocampal cultures were prepared from embryonic day 18 (E18) rat brains. Cells were plated on coverslips coated with poly-L-lysine (30 μg/mL) and laminin (2 μg/mL) at a density of 100,000/well. Hippocampal cultures were grown in Neurobasal medium (NB) supplemented with B27, 0.5 mM glutamine, 12.5 μM glutamate and penicillin/streptomycin. Hippocampal neurons at 19–24DIV were transfected using Lipofectamine 2000 (Invitrogen, Carlsbad, CA). Briefly, DNA (3.6 μg /well) was mixed with 3 μL Lipofectamine 2000 in 200 μL NB, incubated for 30 min and then added to the neurons in NB with 0.5 mM glutamine at 37°C in 5% CO_2 for 60–90 min. Next, neurons were washed with NB and transferred in the original medium at 37°C in 5% CO_2. Two to three days after transfection, neurons were transferred to imaging buffer (NaCl 120, KCl 3, HEPES 10, $CaCl_2$ 2, $MgCl_2$ 2, D-Glucose 10 mM, adjusted to pH 7.35 and 240 mOsm) and imaged for up to 1 h at 37°C and 5% CO_2.

To label the plasma membrane, we generated mem-mEos3.2, a fusion of the green-to-red photoconvertible fluorescent protein mEos3.2 (30) to the carboxy-terminal CAAX motif of hKras (31) by amplifying mEos3.2 using extension PCR (forward primer: 5′-ATGGGGCGCGCCTTAAGATAAAA CACATTTACAAGACATACATCGTCTGGCATTGTCAGGCAATCCAG AATGAG-3′; reverse primer: 5′-CAAGCTAGCGCCACCATGAGTGCG ATTAAGCCAGACATGAA-3′), followed by insertion into the β-actin vector with *Nhe*I and *Asc*I. Farnesyltransferases will modify the CAAX motif with a hydrophobic farnesyl group (prenylation) that will target the protein to cellular membranes.

Live cell imaging

Dendrites were imaged on a TE2000E-based TIRF microscope (Nikon, Tokyo, Japan) equipped with a LightHub4 compact laser combiner (Omicron-

Laserage Laserprodukte, Rodgau, Germany) with LuxX 405 nm 60 mW, LuxX 488 nm 100 mW and Cobolt Jive 561-nm 100-mW lasers (http://www.coboltlasers.com/). The excitation light illuminates the sample in an oblique, near-critical angle through a CFI Apo TIRF 100 × 1.49 N.A. oil objective (Nikon). Images with an effective pixel size of 64 nm were acquired on an Evolve 512 EMCCD camera (Photometrics, Tucson, AZ). The setup also contains a motorized stage (Prior Scientific, Rockland, MD), a Perfect Focus System (Nikon), a quad-band dichroic mirror (C166680; Chroma Technology, Bellows Falls, VT), an incubation chamber (INUBG2E-ZILCS; Tokai Hit, Shizuoka, Japan), and an ILas0 FRAP system (Roper Scientific France, Lisses, France). The software MetaMorph 7.7.6 (Molecular Devices, Sunnyvale, CA) was used to control the camera and all motorized parts.

For diffusion measurements, the center quadrant of the camera was used to record fluorescence images in the 561-nm channel at 50-ms intervals in stream mode. After a baseline measurement of 15 frames, a 405-nm laser pulse was targeted to a diffraction-limited spot in the spine head to induce photoconversion of mEOS3.2 from green to red and the red fluorescence was subsequently followed for 400 frames. The same region of the dendrite was subsequently used for photoactivated localization microscopy (PALM) acquisition at 30-ms intervals for 6000 frames (Fig. 1). The 561- and 405-nm laser intensities were manually increased to achieve optimal photoconversion/bleaching dynamics to detect single molecules.

Image analysis

Images were analyzed and measured in the software ImageJ (National Institutes of Health, Bethesda, MD) and subsequent data analysis, statistical testing, and plotting was carried out in the "R" environment (version 3.0.0; https://www.r-project.org/about.html). Unless otherwise indicated, linear regression coefficients were tested for significance with a two-tailed *t*-test and the obtained variance is indicated as multiple R^2. Significance code used is $0 < *** < 0.001 < ** < 0.01 < * < 0.05 < ns < 1$.

Diffusion measurement analysis. Fluorescence intensities in a region of interest encompassing the entire targeted dendritic spine were background-subtracted with the average of the 15 frames before photoactivation and normalized to the maximum intensity recorded. The resulting intensity curves were fitted with a single exponential function of the form

$$y = ae^{-t/\tau} + b, \tag{1}$$

where t denotes time, τ is the characteristic timescale, and a and b denote amplitude and offset, respectively. To be considered a successful measurement, we applied a cutoff on the acceptable plateau b of 0.2 and only considered fits with $R^2 > 0.7$.

Superresolved morphology analysis. To reconstruct superresolved images of the single molecule localizations, we used a custom-written analysis software DoM (32) (https://github.com/ekatrukha/DoM_Utrecht/). We reconstructed images at 10-nm pixel size after using a correlation-based drift correction in steps of 1000 frames and applying an automated cutoff (~0.3 px) for localization precision. The resulting reconstructions were cropped and binarized by thresholding after removal of background noise, then Gaussian blurring. The base, tip, and head/neck transition point of spines were annotated manually to draw a spline through the major axis of the spine. Subsequently, line scans perpendicular to this axis were taken at every pixel, averaging 10 px each (Fig. 1 *D*). The full width at half-maximum (FWHM) of each linescan was defined as the spine's width at this location. The average of all width measurements along the spine neck and the average of the 10 largest width measurements in the spine head were defined as neck width and head width, respectively. The spine and neck length were given by the length of the splines used for the initial line scans. Spines with a mean head width smaller than 1.5× of the mean neck width were classified as "non-mushroom-shaped" spines.
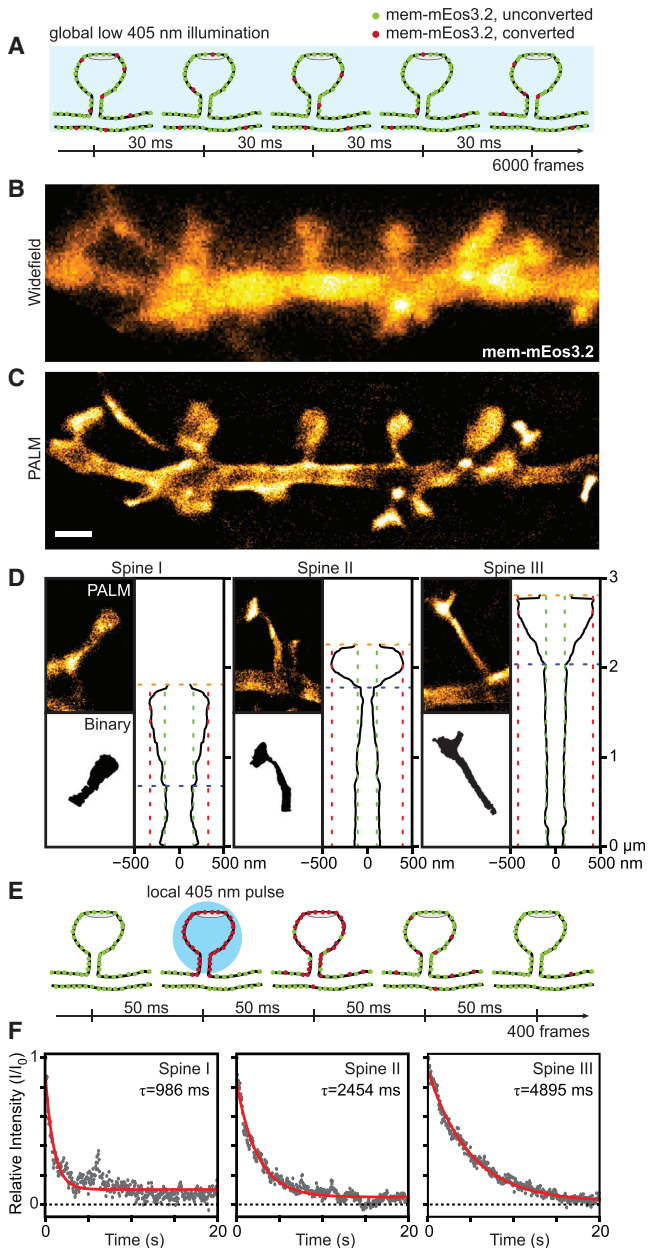
FIGURE 1 Imaging diffusion morphology and membrane-bound diffusion of living dendritic spines. (*A*) Given here is an assay for live PALM imaging of dendritic spines: global low intensity 405 nm illumination results in stochastic photoconversion of mem-mEos3.2 allowing detection of individual molecules for PALM detection over 6000 frames. (*B* and *C*) Given here is a widefield (*B*) and super-resolved (*C*) image of the same dendrite expressing mem-mEos3.2. (*D*) Shown here is the morphology analysis of three dendritic spines. PALM reconstructions (*top*) were binarized (*bottom*) and a spline was fitted through the major axis of each spine. Plotting the FWHM along this axis (*right*) allows reconstructing spine morphology and measuring neck width, head width and spine and neck length. (*E*) Given here is an assay for diffusion measurements: spines were imaged at 561 nm in 50 ms intervals for 400 frames and locally photoconverted after 15 frames with a local laser pulse of 405 nm wavelength. (*F*) Given here are intensity traces of photoconverted mem-mEos3.2 signal over time for the three spines shown in (*D*). The red line indicates fit of exponential decay from which the indicated τ was derived. To see this figure in color, go online.

Simulations

To simulate the role of spine shape on the diffusion of membrane-bound markers, we performed Langevin dynamics simulations using the standard molecular dynamics package LAMMPS (http://lammps.sandia.gov/), supplemented with a RATTLE constraint algorithm to implement a prescribed shape for the dendritic spine (33). We used a Langevin damping time of $\tau = 0.1$ simulation units (SU), and assumed that particles have no mutual interactions. To fit the experimental superresolution data, we parameterized the spine shape using the following function,

$$r^2(x) = \left(k - \frac{x^2}{m^2} \right) \left(1 + \left(A \sin lx^2 \right)^n \right), \qquad (2)$$

where k is the radius of the neck, $k \times m$ equals the height of the spine, and l and A are shape parameters that are optimized to fit the overall shape of the spine. We have used integer values for n, ranging from 1 to 8 to optimally fit the shape of the spine (Fig. 3 *D*). Note here that increasing n increases the curvature at the zone connecting the head and neck. Larger values ($n = 6$–8) typically fit long thin necks with large heads, whereas lower values ($n = 1$–2) suit stubby or thin spines. Spines that had a distinct nonmonotonic increase in radius as function of height could not be fitted with Eq. 2, and were excluded from the analysis.

Once the shape of the spine is created, we prepared the system as follows: the surface of the dendritic spine was uniformly covered with 1000 noninteracting particles, representing the receptor proteins. These particles diffuse across the surface of the spine, and were removed from the system once they exit the base of the spine. We measured the concentration of particles $C(t)$ as function of time t which, similarly to the experiments, decayed exponentially as

$$\frac{C(t)}{C(0)} = e^{-t/\tau}, \qquad (3)$$

where τ is the characteristic timescale of decay, i.e., a measure for the amount of confinement.

To compare the diffusive timescales obtained from the Langevin dynamics simulations with those obtained from the experiments, we needed to relate the simulation units of time and distance from the simulations with those in the experiments. Therefore, we first calculated the mean squared displacement (MSD) for particles on a planar surface with parameters otherwise identical to those in the curved, spine case, and compared this with the experimentally obtained 2D diffusion coefficient of 0.022 μm^2/s. The latter was measured by linking single-molecule localizations from three dendrites into 1044 trajectories, followed by calculating the MSD versus time delay t. Linear fitting of MSD = $4Dt$ to the first three points of the curve (excluding zero) then yielded the estimate for D. In our simulation we have fixed the spatial dimension such that 1 μm corresponds to 10 SU_x (spatial simulation unit: SU). To reach a mean square displacement of $(10\ SU_x)^2$, a particle needed on average 25,000 simulation time steps δt_{sim}, indicating a simulated diffusion coefficient of $10^{-3}\ SU_x{}^2/\delta t_{sim}$ or $10^{-5}\ \mu m^2/\delta t_{sim}$. Hence, δt_{sim} corresponds to $10^{-5}/0.022$ s.

To examine the effects of a difference in diffusion coefficients between the neck and the head of dendritic spines, we locally varied the Langevin damping time τ, a simulation parameter directly proportional to the local diffusion coefficient.

RESULTS

To study how membrane-bound diffusion is influenced by the morphology of dendritic spines, we set up an assay that enabled us to measure membrane-based diffusion in combination with subdiffractive imaging of the shape of

individual spines in living hippocampal neurons. Both measurements are based on a single exogenous probe, mem-mEos3.2, to minimally interfere with the system and to prevent interactions of the probe with other proteins in the spine head (Fig. 1).

Conventional light microscopy cannot accurately resolve the detailed morphology of dendritic spines (Fig. 1 B). The neck of dendritic spines is particularly challenging: typically it has a diameter of 50–200 nm, as measured by electron microscopy (1), which falls below the diffraction limit of fluorescence microscopy. Therefore, we used live PALM (Fig. 1, A and C), allowing us to localize single fluorescent proteins with subdiffraction accuracy, and to reconstruct the images at 10-nm pixel size. These images were further processed to measure the FWHM along the major axis of the spine from which the shape parameters spine length, neck length, head width, and neck width can be extracted (Fig. 1 D).

To correlate spine morphology with the associated equilibration timescale τ, we also measured bulk diffusion in the same spines by photoconversion. Converting the same fluorescent probe mem-mEos3.2 from green to red emission by locally exposing spine heads to a diffraction-limited spot of 405 nm light, we followed the subsequent decay of red fluorescence intensity in the spine over time and fitted the measurements with a single exponential decay function (Fig. 1 E). From this function, we derived the time constant τ as readout for the diffusive timescale of spine equilibration, in which high values for τ indicate slow diffusion rates (Fig. 1 F).

The resulting shape measurements of $n = 128$ spines in $N = 5$ experiments (Fig. 2) are consistent with earlier electron microscopy (EM)-based spine dimensions (1) and with measurements done with STED superresolution microscopy in organotypic and acute slice of mice brains (34) (Fig. 2 I). A small overall increase in the spine dimensions compared to the latter study may be explained by the localization of our probe to the plasma membrane rather than the cytoplasm, resulting in overall widening of the FWHM. No strong interdependence of spine length and neck width or

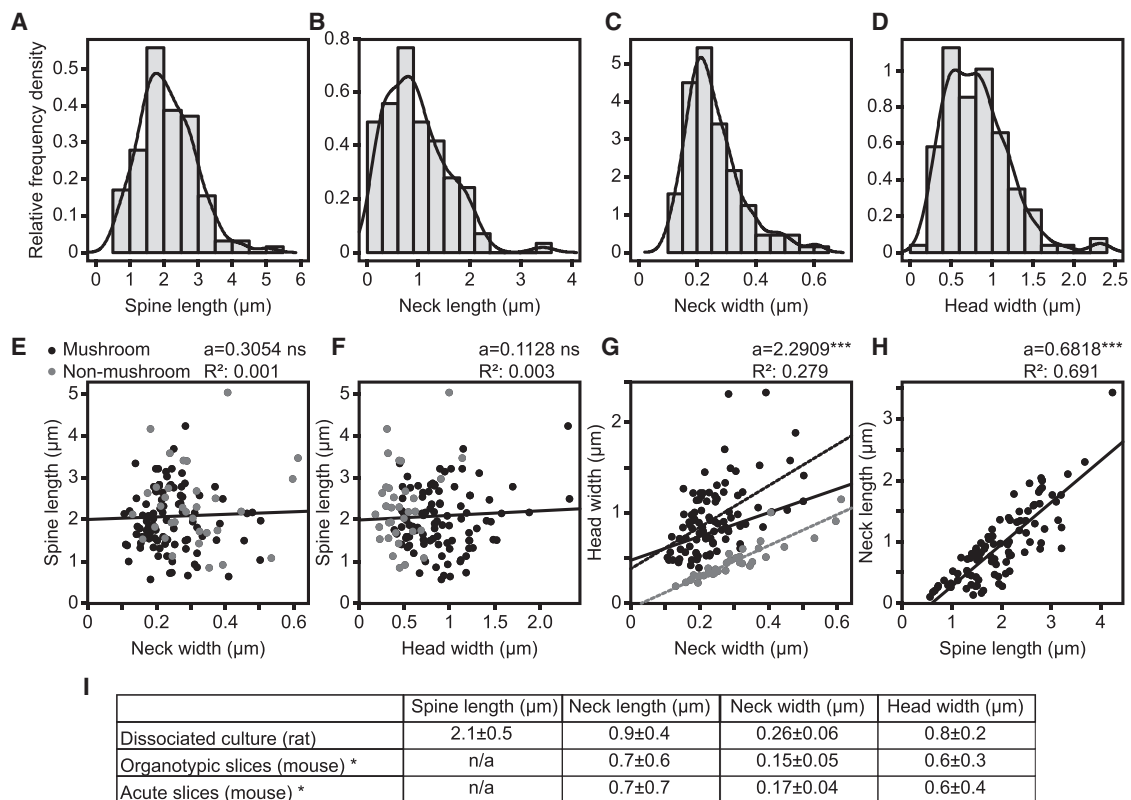|	Spine length (μm)	Neck length (μm)	Neck width (μm)	Head width (μm)
Dissociated culture (rat)	2.1±0.5	0.9±0.4	0.26±0.06	0.8±0.2
Organotypic slices (mouse) *	n/a	0.7±0.6	0.15±0.05	0.6±0.3
Acute slices (mouse) *	n/a	0.7±0.7	0.17±0.04	0.6±0.4

FIGURE 2 Distribution dendritic spine morphology measurements. (A–D) Histograms show the distribution of measured spine lengths (A), neck lengths (B), neck widths (C), and head widths (D) ($n = 128$ spines); the solid line indicates relative frequency density. (E–H) Given here are the correlations of spine morphology parameters against each other. Gray dots indicate non-mushroom-shaped spines spines (mean head width < 1.5 × the mean neck width, $n = 33$), black dots indicate mushroom-shaped spines (all others, $n = 95$). Solid black lines show fitted regression with slope a and goodness of fit as indicated at the top; in (G) black and grey lines show separate regressions for spine subpopulations. (I) Shown here is a comparison of spine morphology measured in this study in dissociated rat hippocampal neurons with live PALM microscopy and spines measured in organotypic and acute slices of mouse hippocampi using STED microscopy. Asterisk (*) indicates datasets published previously (34). Data are shown as mean ± IQR (Q3–Q1) in μm.

head width was observed (Fig. 2, *E* and *F*). Remarkably and contrary to earlier studies (34), we did find a significant correlation between neck width and head width (Fig. 2 *G*). Less surprisingly, neck length and spine length correlated strongly. To compare our results with previous simulation studies (14), we therefore focused on spine length rather than neck length. In conclusion, PALM nanoscopy allowed us to precisely parameterize dendritic spine morphologies of living neurons.

In earlier simulations, we have explored the effect of neck width on τ, while keeping other parameters constant (14,15). We found that τ increased by decreasing the width of the

spine neck. However, increasing the size of the head for a given neck width should also increase τ. Indeed, using a similar approach as in earlier simulations (14,15), we found that, with constant neck width and length, τ scaled nearly linearly with the surface area of the spine head (Fig. 3, *A* and *B*). We also explored the effect of having a different diffusion coefficient in the neck (either two times faster or 10 times slower than elsewhere). For a given spine, this resulted in lower and higher escape times, but it did not change the overall scaling with surface area of the head (Fig. 3 *B*).

To further explore the effect of exact spine shape, we simulated diffusion in spines with the same surface area
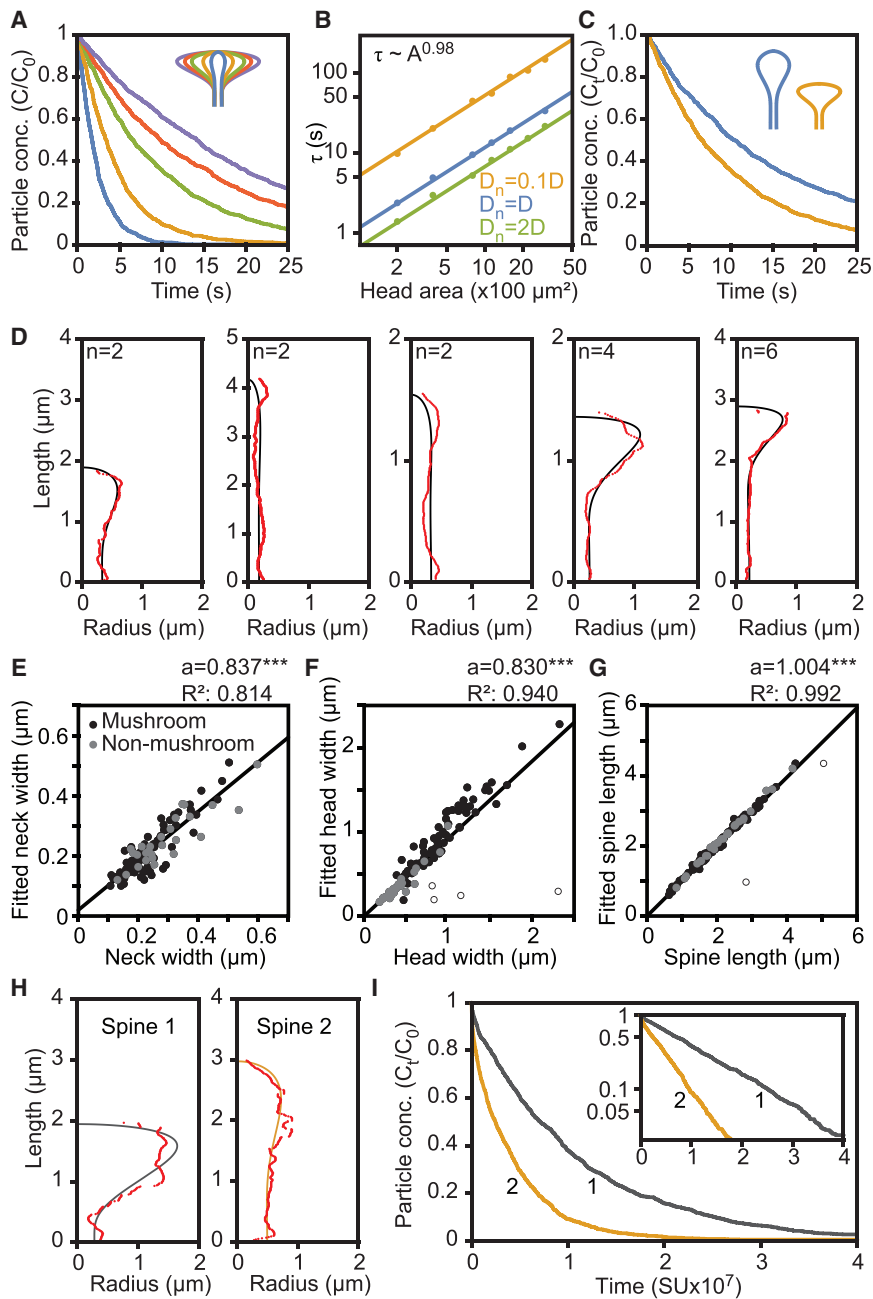

FIGURE 3 Simulation of particle diffusion on spine shapes fitted on measured spine morphologies. (*A*) Shown here is the decay of particle concentration simulated in spines with varying head sizes and surface area. (*B*) Log-log plot of the time constant τ as function of the surface area of the spine head for spines with uniform diffusion or spines with a faster or slower diffusion coefficient in the spine neck is given. (*C*) Shown here is the decay of particle concentration in spines with equal surface area and neck diameter but different overall shape (shown in *inset*). (*D*) Shown here are five examples of measured spine morphology data fitted with a function shown in Eq. 3 (*smooth curve*). For each example, the exponent *n* of the function is given. (*E–G*) Given here are fitted versus measured spine morphology parameters ($n = 100$). Black and gray dots indicate mushroom-shaped ($n = 74$) and non-mushroom-shaped spines ($n = 26$), respectively. Black lines show fitted regression with slope *a* and goodness of fit as indicated at the top. Open circles indicate six outliers that have been excluded from further analysis. (*H*) Given here are examples of measured and fitted (*smooth curve*) morphology profiles for two spines. (*I*) Given here is the decay of particle concentration simulated for the two spine morphologies shown in (*H*). (*Inset*) Given here is the same dataset in a semilog plot. To see this figure in color, go online.

and spine neck thickness, but with a different head shape. For a spine with a given surface area and neck radius, τ could be altered by changing the aspect ratio of the head (i.e., by altering head width and spine length) (Fig. 3 C). Therefore, to directly compare experimental values with the predictions based on simulations, we decided to perform simulations using measured spine morphologies to directly predict τ for specific spines, assuming it is solely governed by its shape, whereas the membrane-bound diffusion constant D is similar in all spines.

Firstly, the width measurements were fitted with the function in Eq. 3 (Fig. 3 D). This function could subsequently be used to generate surfaces of revolution that closely resemble the shape of spines measured initially (see Materials and Methods for details). The fitted spine morphology values closely matched the values from the initial measurements in all but six spines, which were excluded from further analysis (Fig. 3, E–G). Secondly, we used the spine morphology parameters obtained from fitting to perform particle diffusion simulations, starting with a homogenous distribution of particles on the spine surface diffusing until they escape the system at the boundary of the spine neck, as described in Kusters et al. (14). From the decay of particle concentration, the simulated diffusion time constant τ could be derived in the same manner as in the photoconversion experiment (Fig. 3, H and I). Thus, by fitting parameterized surfaces of revolution to spine morphology data, we could execute particle simulations on realistic spine shapes to determine their expected diffusion time constant τ.

We performed these simulation for all $n = 100$ spines that we could fit using Eq. 3 (Fig. 3, E–G). This resulted in a distribution of diffusion time constants with a mean of 1.9 ± 1.5 s (mean $\pm$ SD) ranging from 0.1 to 7.6 s (Fig. 4 A). For the experimentally obtained time constants, the overall distribution was shifted toward higher τ-values and the mean was 2.3 ± 1.0 s in a range from 0.6 to 5.7 s (Fig. 4 B). Plotting the numerically obtained time constant against the experimental values for each spine revealed a good correlation between the two (Fig. 5 C), although the simulated value were often lower than the experimental values, especially for non-mushroom-shaped spines. Indeed, the ratio of experimental and simulated τ showed a frequency density distribution peaking at 1.07, but with a shoulder toward higher values compared to a normal distribution. This indicates that the simulations underestimate the time constants for a subpopulation of spines (i.e., the simulations predict faster diffusion than measured by photoconversion).

Next we examined how the simulated diffusion time constants depended on the morphology parameters used for the simulations. Although τ correlated linearly with spine length and, to a lesser extent, with head width, there was no apparent dependence of the neck width (Fig. 5, A–C). For the experimentally measured diffusion time constants, we did not observe clear correlations (Fig. 5, D–F). This
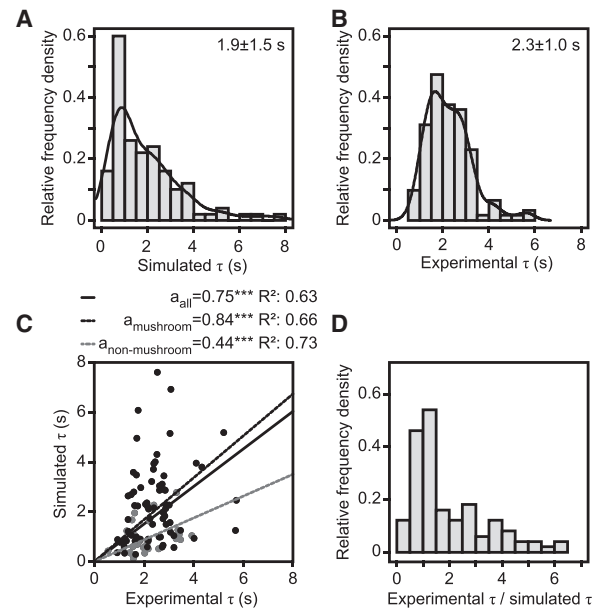

FIGURE 4 Comparison of experimental and simulated diffusion kinetics in dendritic spines. (A and B) Shown here are histograms of simulated (A) and experimentally measured (B) diffusion time constants τ for $n = 100$ and $n = 128$ spines, respectively. Mean $\pm$ SD is indicated. Solid line indicates relative frequency density. (C) Given here is simulated versus measured diffusion time constants τ ($n = 100$). Black and gray dots indicate mushroom-shaped ($n = 74$) and non-mushroom-shaped spines ($n = 26$), respectively. Solid black, dashed black, and dashed gray lines show fitted regressions with their slopes a and goodness of fit indicated at the top for all, mushroom-shaped spines, and non-mushroom-shaped spines, respectively. (D) Shown here is a histogram of the ratio between experimental τ and simulated τ for $n = 100$ spines.

counterintuitive observation results from the multidimensionality of spine morphologies. Whereas in previous simulations all but one of the shape parameters were kept constant (14), in our dataset the correlations for each morphology parameter are confounded by changes in the remaining parameters (e.g., a spine with a thin neck may be shorter than a spine with a wider neck).

To reduce the dimensionality of the problem, we searched to establish a shape factor S that combined the dependence of spine length l_{spine}, head width w_{head}, and neck width w_{neck} in one metric, such that τ is governed by S and D in the following way:

$$\tau[s] = \frac{S[\mu m^2]}{D[\mu m^2/s]}. \quad (4)$$

Considering that the dimension of S should be μm^2 and that increasing l_{spine} and w_{head} should increase τ, whereas increasing w_{head} should decrease τ, we established the following hypothetical dependence:

$$S_a = \frac{l_{spine}^\alpha * w_{head}^\alpha}{w_{neck}^{2\alpha-2}}, \quad (5)$$
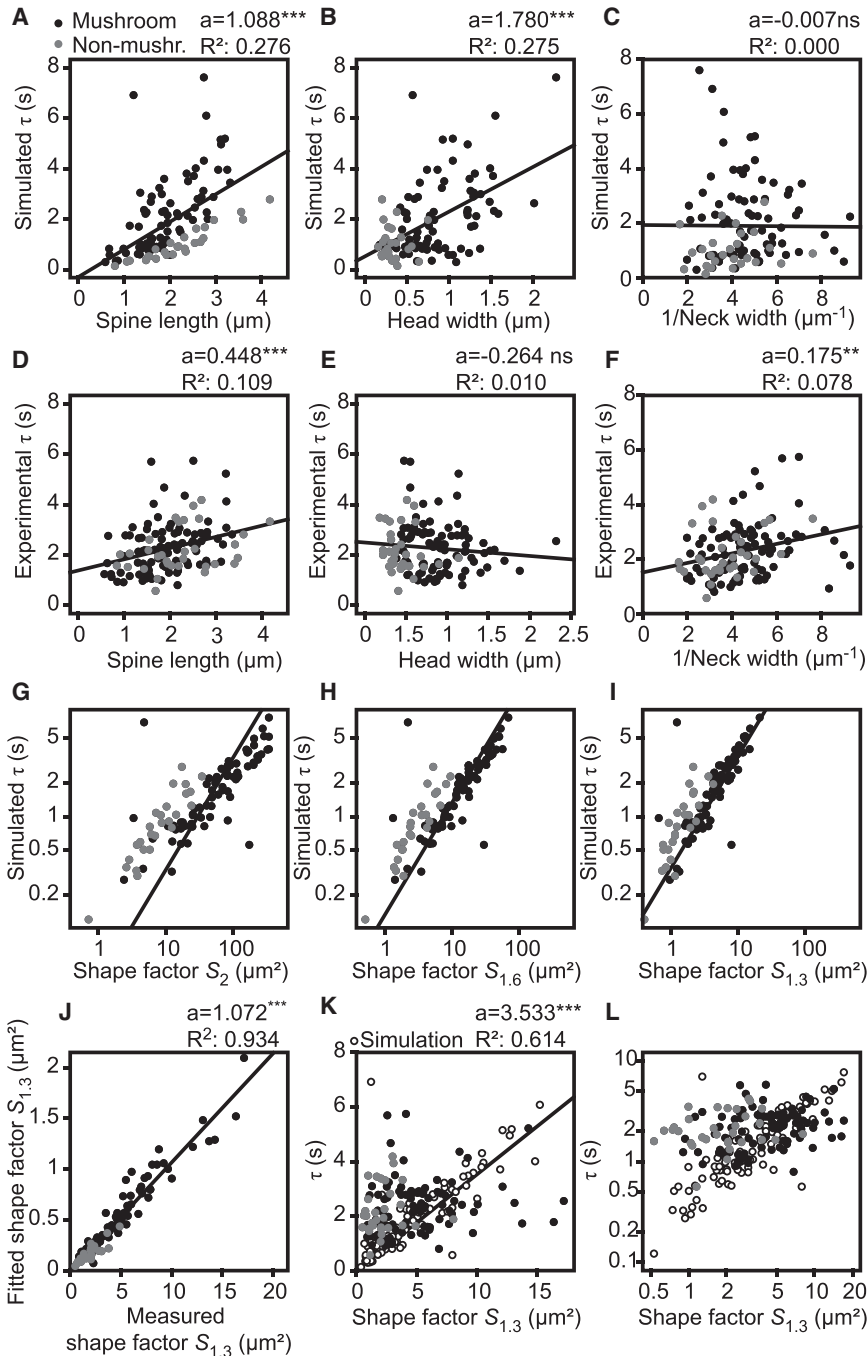
FIGURE 5 Spine morphology sets the lower bound for the diffusion time constant. (*A–F*) Given here are correlations of simulated (*A–C*) and measured (*D–F*) diffusion time constants τ and spine morphology parameters ($n = 100$, 122 spines). Black and gray dots indicate mushroom-shaped and non-mushroom-shaped spines, respectively. Black lines show fitted regression with slope *a* and goodness of fit as indicated at the top. (*G–I*) Shown here are simulated diffusion time constants τ plotted against three different shape factors defined by Eq. 5 using $a = 2$, 1.6, and 1.3, respectively. Black and gray dots indicate mushroom-shaped ($n = 74$) and non-mushroom-shaped spines ($n = 26$), respectively. Black lines with slope of 1 are plotted to illustrate linear dependence. (*J*) Given here are shape factors $S_{1.3}$ derived from measured morphology parameters versus shape factors from morphology parameters obtained from fitting ($n = 100$). Black and gray dots indicate mushroom-shaped ($n = 74$) and non-mushroom-shaped spines ($n = 26$), respectively. Black line shows fitted regression with slope *a* and goodness of fit as indicated at the top. (*K* and *L*) Shown here are the measured diffusion time constants τ ($n = 122$) plotted against the shape factor $S_{1.3}$ on linear (*K*) or logarithmic (*L*) axes. Black and gray dots indicate mushroom-shaped ($n = 74$) and non-mushroom-shaped spines ($n = 26$), respectively. Black lines show fitted regression with slope *a* and goodness of fit indicated at the top. Open circles illustrate τ obtained from simulation versus shape factor $S_{1.3}$ obtained using morphology parameters obtained from fitting.

where α denotes the power of the dependence on l_{spine} and w_{head}. To find the proper value of *a*, we plotted the simulated τ-values, t_{sim}, against the shape factor S_α for $\alpha = 2$, 1.6, and 1.3 and found that this dependence was linear for $\alpha = 1.3$, with most points following this dependence ($R^2 = 0.71$; Fig. 5, *G–J*). Thus, by reducing multiple spine morphology parameters into a single shape factor $S_{1.3}$, we find a clear relation between this shape factor and the simulated diffusion time constant, as we would expect from earlier simulations (14).

Finally, to examine whether the experimentally observed timescale τ_{exp} of membrane-bound diffusion followed a similar dependence on the shape factor, we plotted τ_{exp} against the shape factor $S_{1.3}$ calculated using experimental value for the shape parameters (Fig. 5, *K* and *L*). We found that for most spines the values are scattered in an area whose lower boundary was set by the simulated data points, although for some spines with large heads ($w_{head} > 1.5$ μm) the experimental values were lower than predicted. These results suggest that spine morphology

establishes the lower bound for the time constant of membrane-bound diffusion, but that other mechanisms often limit the diffusive timescale to an even greater extent.

DISCUSSION

Here we use superresolution microscopy of spine morphology and bulk photoconversion of a membrane-bound fluorescent protein, mem-mEos3.2, to examine how spine morphology affects the timescale of diffusive equilibration. Whereas previous work had already established that diffusive equilibration differs between spines, the extent to which this was governed by shape alone had remained unresolved. By comparing the measured time constants with particle simulations carried out on the same spine morphologies, we show that spine morphology determines the lower-bound for diffusive equilibration, but that additional mechanisms slow down equilibration beyond the timescale set by spine shape.

We picked mem-mEos3.2 as membrane-bound probe, both to visualize spine morphology and to measure membrane-bound diffusion. This probe is ideally suited for this assay as it is unlikely to interact with scaffolding proteins in or around the postsynaptic density, as most receptors would. Our imaging approach currently precludes us from obtaining 3D morphology data and therefore we did not have full knowledge of spine morphology and assumed spine geometry to be rotationally symmetrical relative to their central axis. This central axis was not necessarily straight, but could be curved to accommodate for the bending or twitching of spines in the x-y plane. Nevertheless, our morphology data closely correspond with EM and other superresolution fluorescence microcopy studies (1,29,34). Also fluorescence microscopy enabled us to image a larger variety of shapes compared to more labor-intensive EM approaches (16) and, importantly, allowed for imaging live dendrites directly after the photoconversion experiment without any need for fixation or correlative techniques. We chose to measure bulk diffusion using photoconversion, as it closely resembles the simulation approach of particles released homogenously on the spine escaping through the spine neck, and circumvents the challenges associated with measuring single-particle motility on a curved surface (35).

Remarkably, we did not observe a direct correlation between τ and spine neck width, which had been predicted by previous simulation studies (14,16). However, whereas in simulations all spine morphology parameters can be precisely controlled and the neck widths can be changed while keeping other parameters constant, we are bound by experimental values. Interestingly, we found a clear experimental correlation between spine width and neck width, demonstrating that wider heads often come with wider necks (Fig. 2 G). In this way, the increased equilibration due to the wider neck is opposed by a greater head size, which

explains why we did not find a correlation between τ and neck width alone. To circumvent the problem of confounding shape parameters, we defined a shape factor S that combined the expected morphology effects on membrane-bound diffusion. From this, we found that $\tau \sim w_{\mathrm{neck}}^{-0.6}$ and $\tau \sim l_{\mathrm{spine}}^{1.3}$, which is similar to the predictions of earlier simulations (14).

Because for most spines $\tau_{\mathrm{exp}} > \tau_{\mathrm{sim}}$, we conclude that spine morphology establishes the lower bound for the time constant of membrane-bound diffusion, but that other mechanisms often limit the diffusive timescale to a greater extent. The cytoskeleton, especially submembranous actin, influences diffusion through corralling or by anchoring proteins in the plasma membrane (36,37). In axons, it has been convincingly demonstrated that the diffusion of membrane-bound molecules is affected by the periodic submembranous actin-spectrin network (38) and similar actin-based structures have recently been reported in spine necks (39). It has also been shown that the septin family of proteins, and particularly Sept7, hamper the diffusion of transmembrane proteins or proteins anchored to the inner leaflet (40,41). Furthermore, membrane curvature (15,42) or lipid composition (43–45) also influence the effective local diffusion coefficient (40,46), whereas we have mostly used a uniform diffusion coefficient based on single molecule tracking along dendrites and spines (see Materials and Methods). As shown in our simulations in Fig. 3 B, different diffusion coefficients in the neck strongly alter overall equilibration times.

Remarkably, for some spines with large heads ($w_{\mathrm{head}} > 1.5$ μm), the experimental values for τ were lower than predicted, which may be due to insufficient photoconversion as a result of using a near diffraction-limited spot in a large spine. In such a case only a part of the spine surface would be photoconverted, which would hinder comparison with simulations based on homogenous particle distribution. Alternatively, large mature spines might harbor an extensive PSD that excludes diffusion of our probe, effectively lowering the available surface for diffusion.

In summary, this study demonstrates that exact spine morphology contributes to retaining membrane-bound probes. Our results also show that morphology alone does not explain all diffusive behavior of our probe, but likely works in concert with other retention mechanisms mediated by cytoskeletal structures or the lipid composition of the membrane. Together, these mechanisms may be important in compartmentalizing glutamate receptors, ion channels, or membrane-bound signaling proteins in spines according to their synaptic strength and activity levels (17).

AUTHOR CONTRIBUTIONS

ACKNOWLEDGMENTS

REFERENCES

1. Bourne, J. N., and K. M. Harris. 2008. Balancing structure and function at hippocampal dendritic spines. *Annu. Rev. Neurosci.* 31:47–67.

2. Schikorski, T., and C. F. Stevens. 1999. Quantitative fine-structural analysis of olfactory cortical synapses. *Proc. Natl. Acad. Sci. USA.* 96:4107–4112.

3. Arellano, J. I., R. Benavides-Piccione, …, R. Yuste. 2007. Ultrastructure of dendritic spines: correlation between synaptic and spine morphologies. *Front. Neurosci.* 1:131–143.

4. Holtmaat, A., and K. Svoboda. 2009. Experience-dependent structural synaptic plasticity in the mammalian brain. *Nat. Rev. Neurosci.* 10:647–658.

5. Mattison, H. A., D. Popovkina, …, S. M. Thompson. 2014. The role of glutamate in the morphological and physiological development of dendritic spines. *Eur. J. Neurosci.* 39:1761–1770.

6. Hu, H.-T., and Y.-P. Hsueh. 2014. Calcium influx and postsynaptic proteins coordinate the dendritic filopodium-spine transition. *Dev. Neurobiol.* 74:1011–1029.

7. Yuste, R., and T. Bonhoeffer. 2001. Morphological changes in dendritic spines associated with long-term synaptic plasticity. *Annu. Rev. Neurosci.* 24:1071–1089.

8. Opazo, P., and D. Choquet. 2011. A three-step model for the synaptic recruitment of AMPA receptors. *Mol. Cell. Neurosci.* 46:1–8.

9. Ehlers, M. D., M. Heine, …, D. Choquet. 2007. Diffusional trapping of GluR1 AMPA receptors by input-specific synaptic activity. *Neuron.* 54:447–460.

10. Opazo, P., S. Labrecque, …, D. Choquet. 2010. CaMKII triggers the diffusional trapping of surface AMPARs through phosphorylation of stargazin. *Neuron.* 67:239–252.

11. Triller, A., and D. Choquet. 2005. Surface trafficking of receptors between synaptic and extrasynaptic membranes: and yet they do move! *Trends Neurosci.* 28:133–139.

12. Nair, D., E. Hosy, …, J. B. Sibarita. 2013. Super-resolution imaging reveals that AMPA receptors inside synapses are dynamically organized in nanodomains regulated by PSD95. *J. Neurosci.* 33:13204–13224.

13. Hoze, N., and D. Holcman. 2014. Residence times of receptors in dendritic spines analyzed by stochastic simulations in empirical domains. *Biophys. J.* 107:3008–3017.

14. Kusters, R., L. C. Kapitein, …, C. Storm. 2013. Shape-induced asymmetric diffusion in dendritic spines allows efficient synaptic AMPA receptor trapping. *Biophys. J.* 105:2743–2750.

15. Kusters, R., and C. Storm. 2014. Impact of morphology on diffusive dynamics on curved surfaces. *Phys. Rev. E Stat. Nonlin. Soft Matter Phys.* 89:032723.

16. Simon, C. M., I. Hepburn, …, E. De Schutter. 2014. The role of dendritic spine morphology in the compartmentalization and delivery of surface receptors. *J. Comput. Neurosci.* 36:483–497.

17. Adrian, M., R. Kusters, …, L. C. Kapitein. 2014. Barriers in the brain: resolving dendritic spine morphology and compartmentalization. *Front. Neuroanat.* 8:142.

18. Biess, A., E. Korkotian, and D. Holcman. 2007. Diffusion in a dendritic spine: the role of geometry. *Phys. Rev. E Stat. Nonlin. Soft Matter Phys.* 76:021922.

19. Holcman, D., and Z. Schuss. 2011. Diffusion laws in dendritic spines. *J. Math. Neurosci.* 1:10.

20. Yuste, R. 2013. Electrical compartmentalization in dendritic spines. *Annu. Rev. Neurosci.* 36:429–449.

21. Araya, R., T. P. Vogels, and R. Yuste. 2014. Activity-dependent dendritic spine neck changes are correlated with synaptic strength. *Proc. Natl. Acad. Sci. USA.* 111:E2895–E2904.

22. Noguchi, J., M. Matsuzaki, …, H. Kasai. 2005. Spine-neck geometry determines NMDA receptor-dependent Ca^{2+} signaling in dendrites. *Neuron.* 46:609–622.

23. Bloodgood, B. L., and B. L. Sabatini. 2005. Neuronal activity regulates diffusion across the neck of dendritic spines. *Science.* 310:866–869.

24. Svoboda, K., D. W. Tank, and W. Denk. 1996. Direct measurement of coupling between dendritic spines and shafts. *Science.* 272:716–719.

25. Ashby, M. C., S. R. Maier, …, J. M. Henley. 2006. Lateral diffusion drives constitutive exchange of AMPA receptors at dendritic spines and is regulated by spine morphology. *J. Neurosci.* 26:7046–7055.

26. Hugel, S., M. Abegg, …, R. A. McKinney. 2009. Dendritic spine morphology determines membrane-associated protein exchange between dendritic shafts and spine heads. *Cereb. Cortex.* 19:697–702.

27. Harvey, C. D., R. Yasuda, …, K. Svoboda. 2008. The spread of Ras activity triggered by activation of a single dendritic spine. *Science.* 321:136–140.

28. Brown, S.-A., F. Morgan, …, L. M. Loew. 2008. Analysis of phosphatidylinositol-4,5-bisphosphate signaling in cerebellar Purkinje spines. *Biophys. J.* 95:1795–1812.

29. Bethge, P., R. Chéreau, …, U. V. Nägerl. 2013. Two-photon excitation STED microscopy in two colors in acute brain slices. *Biophys. J.* 104:778–785.

30. Zhang, M., H. Chang, …, T. Xu. 2012. Rational design of true monomeric and bright photoactivatable fluorescent proteins. *Nat. Methods.* 9:727–729.

31. Hancock, J. F., H. Paterson, and C. J. Marshall. 1990. A polybasic domain or palmitoylation is required in addition to the CAAX motif to localize p21ras to the plasma membrane. *Cell.* 63:133–139.

32. Chazeau, A., E. A. Katrukha, …, L. C. Kapitein. 2016. Studying neuronal microtubule organization and microtubule-associated proteins using single molecule localization microscopy. *Methods Cell Biol.* 131:127–149.

33. Paquay, S., and R. Kusters. 2016. A method for molecular dynamics on curved surfaces. *Biophys. J.* 110:1226–1233.

34. Tønnesen, J., G. Katona, …, U. V. Nägerl. 2014. Spine neck plasticity regulates compartmentalization of synapses. *Nat. Neurosci.* 17:678–685.

35. Oswald, F., E. L M Bank, …, E. J. G. Peterman. 2014. Imaging and quantification of trans-membrane protein diffusion in living bacteria. *Phys. Chem. Chem. Phys.* 16:12625–12634.

36. Honkura, N., M. Matsuzaki, …, H. Kasai. 2008. The subspine organization of actin fibers regulates the structure and plasticity of dendritic spines. *Neuron.* 57:719–729.

37. Korobova, F., and T. Svitkina. 2010. Molecular architecture of synaptic actin cytoskeleton in hippocampal neurons reveals a mechanism of dendritic spine morphogenesis. *Mol. Biol. Cell.* 21:165–176.

38. Albrecht, D., C. M. Winterflood, …, H. Ewers. 2016. Nanoscopic compartmentalization of membrane protein motion at the axon initial segment. *J. Cell Biol.* 215:37–46.

39. Bär, J., O. Kobler, …, M. Mikhaylova. 2016. Periodic F-actin structures shape the neck of dendritic spines. *Sci. Rep.* 6:37136.

40. Ewers, H., T. Tada, …, D. Choquet. 2014. A septin-dependent diffusion barrier at dendritic spine necks. *PLoS One.* 9:e113916.

41. Tada, T., A. Simonetta, …, M. Sheng. 2007. Role of septin cytoskeleton in spine morphogenesis and dendrite development in neurons. *Curr. Biol.* 17:1752–1758.

42. Domanov, Y. A., S. Aimon, …, P. Bassereau. 2011. Mobility in geometrically confined membranes. *Proc. Natl. Acad. Sci. USA.* 108:12605–12610.

Adrian et al.

43. Ueda, Y., and Y. Hayashi. 2013. PIP$_3$ regulates spinule formation in dendritic spines during structural long-term potentiation. *J. Neurosci.* 33:11040–11047.

44. Fukata, Y., A. Dimitrov, …, M. Fukata. 2013. Local palmitoylation cycles define activity-regulated postsynaptic subdomains. *J. Cell Biol.* 202:145–161.

45. Hering, H., C.-C. Lin, and M. Sheng. 2003. Lipid rafts in the maintenance of synapses, dendritic spines, and surface AMPA receptor stability. *J. Neurosci.* 23:3262–3271.

46. Shim, S.-H., C. Xia, …, X. Zhuang. 2012. Super-resolution fluorescence imaging of organelles in live cells with photoswitchable membrane probes. *Proc. Natl. Acad. Sci. USA.* 109:13978–13983.